Travel Time Computation in Snow and Ice Volumes for Radar Remote Sensing Applications

Andreas Benedikter, *Member, IEEE*, Christian Huber, *Member, IEEE*, Letizia Gambacorta, Marc Rodriguez-Cassola, and Gerhard Krieger, *Fellow, IEEE*

***Abstract*— When radar signals penetrate snow and ice, they experience additional delays and directional changes due to the higher refractive index compared to that of air. These propagation effects should be taken into account accurately when processing, simulating, or geocoding radar data. Travel time computation is straightforward when the refractive index is constant, but it becomes challenging in heterogeneous media. This letter introduces novel methods based on the Eikonal equation and Fermat's principle for efficiently computing radar signal travel times in heterogeneous snow and ice volumes. These approaches can accommodate nearly arbitrary refractive index distributions, ensuring precise handling of propagation effects in radar remote sensing applications.**

***Index Terms*— Ice, propagation effects, radar, refraction, snow, synthetic aperture radar (SAR).**

I. Introduction

RADAR signals partially penetrate semitransparent media such as snow, firn, and ice, allowing imaging of structures and processes within or beneath snow covers, ice sheets, or glaciers. When radar waves propagate into glacial volumes, the increased refractive index reduces the propagation velocity of the signals and alters the direction of the Poynting vector (i.e., the direction of energy flux). These changes occur as a result of refraction at dielectric interfaces and bending along refractive index gradients. Properly accounting for these propagation effects is relevant for processing, interpreting, and accurately simulating low-frequency radar data acquired from various sensors, including radar sounders, and synthetic aperture radar (SAR) systems [1], [2], [3], [4]. Not accurately accounting for additional signal delays and directional changes can lead to data misinterpretation, geolocation errors, and defocusing in processed and simulated imagery [5], [6].

Propagation effects can be accommodated by correctly computing the travel time of the radar signal (i.e., the optical path length) between the sensor and target positions. The computation is trivial for propagation in homogeneous dielectric media with constant refractive index but becomes challenging in heterogeneous media. For snow and ice environments, in addition to the dielectric contrast formed by the interface between air and the glacial volume, the contrast or gradual variation of the subsurface density or liquid water content forms a medium with a heterogeneous refractive index distribution [7]. A common simplification made in radar remote sensing applications is to treat the glacial volume as a vertically stratified refractive index distribution (see, e.g., [2]), or as a single layer, resulting in a two-layer medium of air and ice [1], [3], [4]. Vertically stratified models cannot account for horizontal refractive index variations and discontinuities along interfaces with strong topography. In this letter, we propose efficient travel time computation methods based on Fermat's principle of least time as well as a numerical solution of the Eikonal equation, capable of accommodating almost arbitrary refractive index distributions. The approaches are inspired by seismic ray tracing and travel time inversion algorithms. Section II of this letter outlines the developed approaches, including a discussion on accuracy and computational complexity. As a potential application scenario, in Section III, the developed approaches are used for simulating the response of a point target located within a heterogeneous glacial volume. Conclusions are drawn in Section IV.

Received 28 January 2025; revised 18 March 2025; accepted 14 April 2025. Date of publication 16 April 2025; date of current version 29 April 2025. *(Corresponding author: Andreas Benedikter.)*

Andreas Benedikter and Marc Rodriguez-Cassola are with the Microwaves and Radar Institute, German Aerospace Center (DLR), 82234 Weßling, Germany (e-mail: andreas.benedikter@dlr.de).

Christian Huber and Letizia Gambacorta are with the Institute of Microwaves and Photonics (LHFT), Friedrich-Alexander University Erlangen-Nürnberg (FAU), 91058 Erlangen, Germany.

Gerhard Krieger is with the Microwaves and Radar Institute, German Aerospace Center (DLR), 82234 Weßling, Germany, and also with the Institute of Microwaves and Photonics (LHFT), Friedrich-Alexander University Erlangen-Nürnberg (FAU), 91058 Erlangen, Germany.

Digital Object Identifier 10.1109/LGRS.2025.3561654

II. Efficient Travel Time Computation

The fundamental principle in travel time computation is the Eikonal equation. As a link between wave propagation and geometrical optics, the Eikonal equation describes wavefronts of constant travel time propagating through a dielectric heterogeneous medium described by the refractive index distribution $n(\vec{x})$ [8]

$$\left|\nabla T(\vec{x})\right| = \frac{n(\vec{x})}{c_0} \tag{1}$$

where ∇ symbolizes the gradient, $T(\vec{x})$ is the travel time field, and c_0 is the speed of light in free space. The Eikonal equation is a high-frequency approximation of the wave equation, valid when $n(\vec{x})$ varies over spatial scales much larger than the wavelength, and when dielectric discontinuities are significantly larger than the wavelength. For ice sheets and glaciers, it may be assumed that the $n(\vec{x})$ variations occur in most cases on a large spatial scale relative to radar wavelengths (a standard assumption in describing radar signal propagation effects [1], [2], [3], [4], [5], [6]), or are significantly smaller (e.g., the packing of the individual ice grains) to be interpreted as a homogeneous mixed medium with an average refractive index. One interpretation of the Eikonal equation is Fermat's principle of least time, which states that the path a ray follows between two points in a heterogeneous medium is

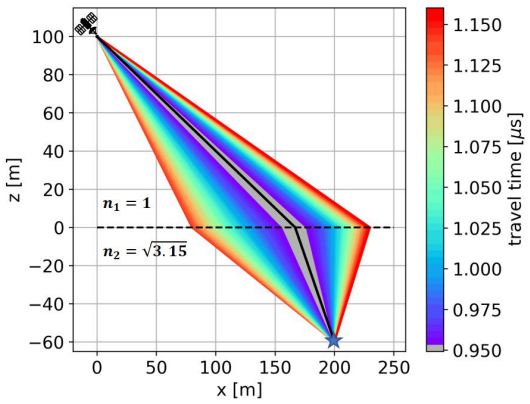

Fig. 1. Travel time along multiple adjacent paths that connect the sensor, a point on an interface (dashed line), and the target. The solid black line represents the path of least travel time, simultaneously satisfying Snell's law.

the one that takes the least time compared to nearby paths. By applying calculus of variations (indicated by δ in the following equation), the physical travel time between two points, P_1 and P_2, is found to minimize the travel time relative to adjacent paths [8]:

$$\delta T = \delta \frac{1}{c_0} \int_{P_1}^{P_2} n(\vec{x})\, ds = 0. \tag{2}$$

A direct consequence of Fermat's principle is Snell's law that describes the refraction effect at dielectric interfaces [8]. The relation between Fermat's principle and Snell's law is illustrated in Fig. 1, showing the travel time along multiple adjacent paths that connect the sensor, a point on an interface (dashed line), and the target. The two media are characterized by constant refractive indices $n_1 = 1$ and $n_2 = \sqrt{3.15}$, corresponding to air and solid ice, respectively. The solid black line represents the path of least travel time, which simultaneously satisfies Snell's law.

Travel time computation methods can be divided into two major categories: ray tracing methods and methods which are based on numerically solving the Eikonal equation (from here on referred to as Eikonal solver). Ray tracing methods are highly accurate and can be efficiently used in vertically stratified $n(\vec{x})$ models with moderate topography of the layer interfaces. For more complex $n(\vec{x})$ distributions that cannot be accommodated unambiguously by ray tracing methods, efficient Eikonal solvers can be implemented to compute the travel times to any point in the analyzed propagation volume.

A. Computation in Vertically Stratified Ice Models

In vertically stratified $n(\vec{x})$ distributions (see Fig. 2), ray tracing methods can be efficiently implemented. For a model with two layers and a straight interface, the intersect point on the interface can be found analytically, but requires solving of a fourth-order polynomial [3]. For stratified models with an arbitrary number of interfaces (see Fig. 2), the travel time can be computed by iteratively varying the intersect points on the interfaces until the overall ray path satisfies Fermat's principle or Snell's law. An efficient implementation is to use gradient-based optimization strategies to find the minimum travel time according to Fermat's principle. The correct ray

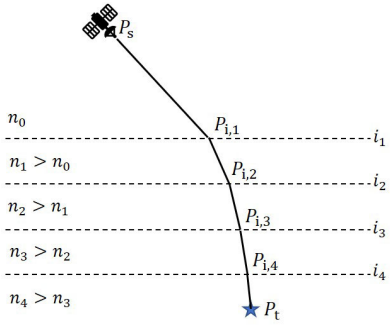

Fig. 2. Layered ice model showing an example of a ray path between the sensor and the target through multiple layers.

path is found by solving

$$\begin{aligned} \min_{\vec{P}_{i,m}} T(\vec{P}_{i,m}) = \min_{\vec{P}_{i,m}} & \left\| \vec{P}_{i,1} - \vec{P}_s \right\|_2 \cdot \frac{n_0}{c_0} \\ & + \sum_{m=1}^{M-1} \left\| \vec{P}_{i,m+1} - \vec{P}_{i,m} \right\|_2 \cdot \frac{n_m}{c_0} \\ & + \left\| \vec{P}_t - \vec{P}_{i,M} \right\|_2 \cdot \frac{n_M}{c_0} \end{aligned} \tag{3}$$

where $\vec{P}_{i,m}$ are the intersect points on the interfaces, $\vec{P}_s$ and $\vec{P}_t$ are the sensor and target position, respectively, n_m are the refractive indices of the layers, and $\|\cdot\|_2$ is the Euclidean norm. The suggested approach is only applicable in scenarios with a moderate topography of the interfaces, e.g., straight or curved interfaces with mild undulations. In such scenarios, the travel time can be computed with an arbitrary accuracy. For a significant topography, multiple local travel time minima occur, not allowing for an unambiguous computation.

B. Computation in Arbitrary Dielectric Distributions

For more complex $n(\vec{x})$ distributions, a direct solving of the Eikonal equation in (1) may allow for an accurate computation of the travel time. In contrast to ray tracing approaches that compute the travel time between two points, Eikonal solvers compute the travel time on a grid, starting from a source point or a wavefront with known travel time. In 1996, Sethian [9] proposed the so-called fast-marching-method (FMM) as an efficient Eikonal solver for seismic imaging. The FMM can be equivalently applied for the case of electromagnetic waves in radar applications. In addition to the local solution of the Eikonal equation using finite differences, the FMM advances the wavefront toward the least travel time according to Fermat's principle. For this reason, the FMM grid is divided into accepted points, points on the advancing wavefront, and far away points (illustrated for a 2-D scenario in Fig. 3). Starting from a source point or a wavefront with known travel times, the algorithm of the FMM proceeds as follows.

1) Choose the point on the wavefront with the smallest travel time and set this point as accepted.
2) Advance the wavefront beyond the selected point (a reinitialization of the points that form the wavefront), such that this point is behind the wavefront and all adjacent points are either on the wavefront or behind it.
3) Update the travel times of the adjacent points on the wavefront by locally solving (1) numerically.

4) Repeat all steps until every point is accepted.

The travel time update in Step 3) is performed by solving (1) using a finite difference scheme, which can be written in form of the following quadratic equation for the travel time T:

$$\begin{aligned}&\max\left(D_{ijk}^{-x}T,0\right)^2+\min\left(D_{ijk}^{+x}T,0\right)^2\\&\quad+\max\left(D_{ijk}^{-y}T,0\right)^2+\min\left(D_{ijk}^{+y}T,0\right)^2\\&\quad+\max\left(D_{ijk}^{-z}T,0\right)^2+\min\left(D_{ijk}^{+z}T,0\right)^2=s_{ijk}^2\end{aligned}\tag{4}$$

where D_{ijk}^{-x} is a backward finite difference operator in x-direction at the grid point with indices i, j, k and D_{ijk}^{+x} is a forward difference operator in x-direction. The finite difference operators in y-direction and z-direction are defined analogously. $s_{ijk} = (n_{ijk}/c_0)$ indicates the slowness of the medium at the grid point i, j, k. The formulation in (4) represents a so-called upwind scheme; it chooses grid points in the finite difference approximation in terms of the direction of the flow of information [9]. A quadratic equation of the form

$$aT^2+bT+c=0\tag{5}$$

can be solved explicitly. Therefore, for solving (4), the coefficients a, b, c need to be accumulated from the nonzero terms in (4) and inserted into (5). The simplest way is to choose a two-point finite difference operator, such as

$$D_{ijk}^{-x}T=\frac{T_{ijk}-T_{(i-1)jk}}{\Delta x}\tag{6}$$

$$D_{ijk}^{+x}T=\frac{T_{(i+1)jk}-T_{ijk}}{\Delta x}\tag{7}$$

which, after squaring (6) and expanding it, results in

$$\left(D_{ijk}^{-x}T\right)^2=\alpha T_{ijk}^2+\beta T_{ijk}+\gamma\tag{8}$$

for the backward operator, where $\alpha = (1/\Delta x^2)$, $\beta = -2T_{(i-1)jk}\alpha$, and $\gamma = T_{(i-1)jk}^2\alpha$, with Δx as the grid spacing. The coefficients a, b, c in (5) can now be calculated as

$$a=\sum_l \alpha_l,\quad b=\sum_l \beta_l,\quad c=\sum_l \gamma_l - s_{ijk}^2\tag{9}$$

where the summation index l refers to the six terms in (4). In Fig. 4, the FMM was applied for a point source located in a 3-D $n(\vec{x})$ distribution (a 2-D slice through the volume is shown). The black contours indicate the wavefronts of constant travel time. Note the distinctive bending effect of the wavefronts.

1) Notes on Accuracy and Computational Complexity: The accuracy of the FMM depends on the grid spacing, with finer grids not only leading to greater precision but also increasing computational complexity. The accuracy can also be enhanced by employing higher order finite-difference schemes and incorporating additional computational directions (i.e., multiple stencils), by including diagonal points in the local travel time calculations. We suggest using a second-order multistencil FMM (MSFMM), as outlined in [10]. To assess the accuracy of the FMM for radar applications, the MSFMM is applied on a point source that is located within well-defined 3-D $n(\vec{x})$ distributions that allow for a closed-form solution of the travel time field. One trivial distribution is chosen

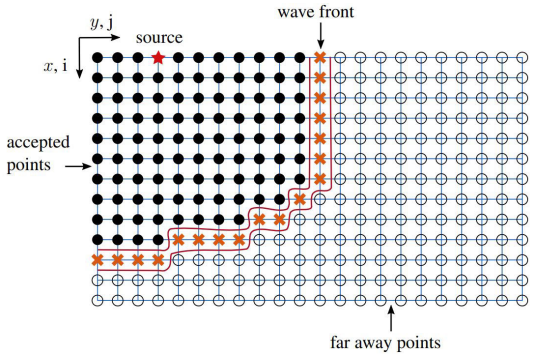

Fig. 3. Illustration of the FMM algorithm, showing the advancing wavefront through a 2-D grid, starting from a source point.

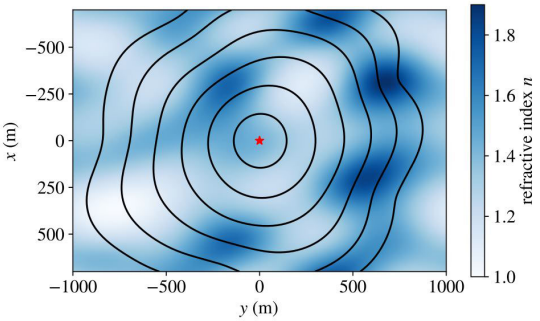

Fig. 4. Simulation of propagating wavefronts through a complex refractive index distribution using the FMM. The range of refractive index values is representative for snow and ice environments. Note the bending effect toward fast regions of the propagation medium.

with $n_1(\vec{x}) = 1$ and a more complex one, $n_2(\vec{x})$, described by sinusoidal variations, shown in Fig. 5(a). The source for the travel time computation is located in the center and the MSFMM is applied on a grid with a 1 m spacing. The resulting travel time error when comparing the MSFMM results and the analytic travel time is shown in Fig. 5(b) for $n_1(\vec{x})$ and in Fig. 5(c) for $n_2(\vec{x})$. The error does not exceed few tens of picoseconds, corresponding to range errors of few centimeters. To precisely accommodate the travel time in the simulation or processing of radar data, phase errors should be kept below $(\pi/4)$ to avoid artifacts when coherently combining multiple echoes [11]. This corresponds to an equivalent ranging error of $(\lambda/16)$. For the 1 m grid in the present example, this requirement is fulfilled for commonly used frequencies in ice penetrating radar remote sensing applications, e.g., up to the L band. The complexity of the FMM algorithm is $\mathcal{O}(N \log N_{\text{wf}})$, where N is the number of grid points and N_{wf} is the maximum number of points forming the advancing wavefront. On a standard portable machine with a 13th Gen Intel[1] Core[2] i7-1370P 1.90 GHz CPU, our implementation of the MSFMM in C++ takes about 1 s to solve the travel time on a 3-D grid with 300^3 points.

2) Practical Implementation Considerations: In radar remote sensing applications, the sensor is typically positioned hundreds of meters to hundreds of kilometers above the surface. The travel time to the surface can be calculated under the assumption of free space propagation. The FMM is then used to compute the propagation within the glacial volume,

[1]Registered trademark.
[2]Trademarked.

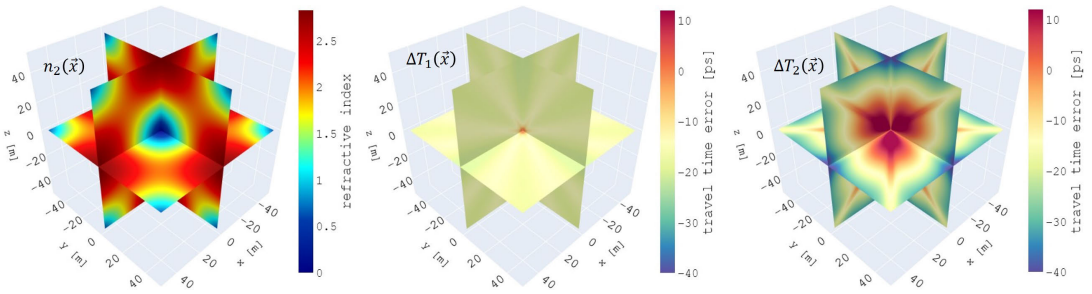

Fig. 5. Accuracy of the MSFMM for the constant refractive index distribution, $n_1(\vec{x})$, and the more complex distribution (a) $n_2(\vec{x})$. The travel time errors, when compared to the analytic travel time, is shown for: (b) $n_1(\vec{x})$ distribution and (c) $n_2(\vec{x})$ distribution.

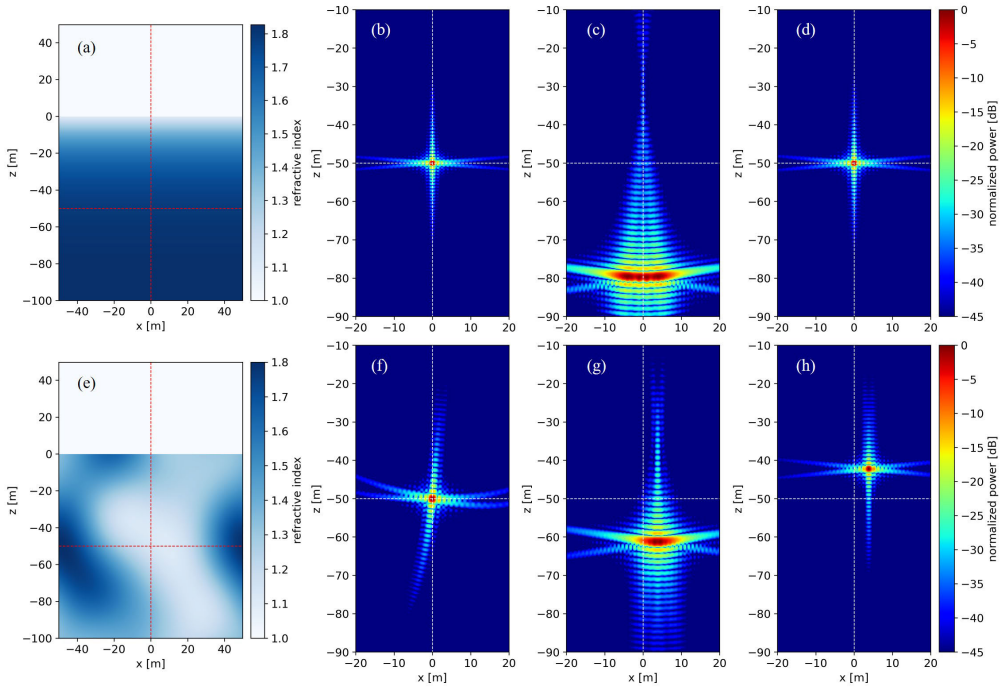

Fig. 6. Results of a radar sounder point target simulation for a target 50 m below the surface located at the intersection of the dashed lines in the $n(\vec{x})$ distributions shown in (a) and (e), showing the target responses when: (b) and (f) assuming the correct $n(\vec{x})$ in the focusing, (c) and (g) assuming propagation in free space, and (d) and (h) assuming the mean $n(\vec{x})$ (formed from the surface to the target position).

accounting also for the refraction at the surface interface. Two approaches can be employed, depending on the specific application as follows.

1) The travel time is computed from a single sensor position to all grid points in the volume of interest. This involves constructing a wavefront of constant travel time above the subsurface volume, which is then propagated using the FMM.
2) The travel time is calculated from a single target to multiple sensor positions. A wavefront is advanced from the target until an area above the surface, where the travel times are combined with those to the sensor positions according to Fermat's principle. Note that also areas of constant $n(\vec{x})$ within the subsurface volume (e.g., deep regions in glaciers and ice consisting purely of solid ice) can be accommodated in a similar manner to reduce the overall computational complexity.

III. Point Target Simulation

As an additional accuracy assessment and as an application example, we conducted a point target simulation for an airborne P-band radar sounder, including SAR focusing. The focusing performance and its sensitivity to various processing assumptions are assessed in this context. SAR focusing at fine resolution is highly sensitive to inconsistencies in the travel time calculation and inaccuracies are commonly easy to spot. The simulation parameters are depicted in Table I. Despite the nadir-looking sounder geometry, the travel times are computed over 3-D volumes to accommodate propagation effects in horizontally heterogeneous $n(\vec{x})$ distributions. The results are shown as 2-D slices through the volume at the target position, where the x-axis corresponds to the azimuth coordinate and the z-axis describes the vertical dimension.

TABLE I
Simulation Parameters

Parameter	Value	Parameter	Value
frequency	435 MHz	target depth	50 m
bandwidth	100 MHz	sensor altitude	4 km
azimuth resolution	1 m	sensor trajectory	straight, horizontal

In a first simulation scenario [see Fig. 6(a)–(d)], a glacial volume with vertically increasing $n(\vec{x})$ is selected (a), with

values ranging from dry snow to solid ice. The vertical distribution allows for calculating the travel time using the approach based on Fermat's principle (see Section II-A), providing arbitrary accuracy. The raw data of the point target are simulated using Fermat's principle, while the travel times for focusing are computed using the MSFMM approach. The focusing is performed via a time-domain back-projection algorithm to account for the varying propagation delays. More efficient implementations in the Fourier domain could be used by accommodating the propagation delays in a similar manner as in motion compensation algorithms used in airborne SAR surveys [12]. Fig. 6(b) shows the focused point target assuming the correct $n(\vec{x})$ distribution for focusing. The target focuses perfectly to the expected resolution, demonstrating that the MSFMM provides sufficient accuracy in the travel time computation. In Fig. 6(c), free-space propagation (i.e., $n(\vec{x}) = 1$) is assumed for focusing. Two effects are observed: 1) a range shift of the point target response due to the uncompensated bulk range delay caused by the higher $n(\vec{x})$; and 2) significant defocusing in the azimuth direction resulting from the uncompensated azimuth-variant delay, which introduces additional quadratic components [5]. The defocusing worsens with finer azimuth resolution. Fig. 6(d) illustrates the result when a constant $n(\vec{x})$ (equal to the mean $n(\vec{x})$ up to the target) is assumed during focusing. Negligible offset or defocusing occurs, indicating that a vertically varying $n(\vec{x})$ distribution is well approximated by a mean value. Note that the mean value must be adjusted for targets at different depths.

In a second simulation scenario [see Fig. 6(e)–(h)], a glacial volume with a more complex $n(\vec{x})$ distribution is considered (e), including also lateral variations. The values are chosen in a range that is typical for dry snow and ice. Strong lateral variations may arise from significant topography or features such as crevasses, which could be filled with snow. In this scenario, travel times for both raw data simulation and focusing are computed using the MSFMM approach (see Section II-B). Fig. 6(f) shows the focused target when assuming the correct $n(\vec{x})$ distribution during focusing. The target focuses to nearly the expected azimuth resolution, as would occur in free space. A slight degradation in resolution can be attributed to a lens-like effect caused by the variations in $n(\vec{x})$. The curvature of the sidelobe pattern is likely due to the bending effect of the $n(\vec{x})$ distribution. In Fig. 6(g), free space propagation is assumed for the focusing, resulting in shifts and a defocusing of the target. In addition to the range shift observed in the scenario of Fig. 6(c), lateral variations in $n(\vec{x})$ also cause an azimuth shift. Fig. 6(h) illustrates the result when a constant $n(\vec{x})$, corresponding to the mean value above the target (up to the surface), is assumed during focusing. Given the lateral variations in $n(\vec{x})$, this mean-value approximation is inadequate, resulting in noticeable shifts.

IV. Conclusion

Inspired by algorithms developed for seismic imaging, we have proposed efficient approaches for calculating the radar signal travel time in media with almost arbitrary refractive index distributions. The proposed approaches are based on a numerical solution of the Eikonal equation and Fermat's principle of least time and can be applied in radar remote sensing applications to describe the propagation through heterogeneous snow and ice volumes (e.g., glaciers or ice sheets), for providing an accurate processing, simulation, and geocoding of ice-penetrating radar acquisitions. It is important to note that in many real-world scenarios, complex travel time computation approaches for the processing of real data do not provide additional value due to a lack of a priori knowledge on the subsurface refractive index distribution. We expect that the main application of the approaches is in the accurate simulation of propagation effects, aiding in the interpretation of data and performance assessment of sensors and processing assumptions. Another application is in the field of radar travel time tomography, as conducted during the Rosetta mission [13] and proposed in [14]. Beyond snow and ice, the developed approaches may be also used to accommodate propagation effects in dry soil, sand, or the atmosphere.

References

[1] A. Heister and R. Scheiber, "Coherent large beamwidth processing of radio-echo sounding data," *Cryosphere*, vol. 12, no. 9, pp. 2969–2979, Sep. 2018.

[2] C. Gerekos, A. Tamponi, L. Carrer, D. Castelletti, M. Santoni, and L. Bruzzone, "A coherent multilayer simulator of radargrams acquired by radar sounder instruments," *IEEE Trans. Geosci. Remote Sens.*, vol. 56, no. 12, pp. 7388–7404, Dec. 2018.

[3] F. Heliere, C.-C. Lin, H. Corr, and D. Vaughan, "Radio echo sounding of pine island glacier, west antarctica: Aperture synthesis processing and analysis of feasibility from space," *IEEE Trans. Geosci. Remote Sens.*, vol. 45, no. 8, pp. 2573–2582, Aug. 2007.

[4] S. Tebaldini, T. Nagler, H. Rott, and A. Heilig, "Imaging the internal structure of an Alpine glacier via L-band airborne SAR tomography," *IEEE Trans. Geosci. Remote Sens.*, vol. 54, no. 12, pp. 7197–7209, Dec. 2016.

[5] A. Benedikter, M. Rodriguez-Cassola, F. Betancourt-Payan, G. Krieger, and A. Moreira, "Autofocus-based estimation of penetration depth and permittivity of ice volumes and snow using single SAR images," *IEEE Trans. Geosci. Remote Sens.*, vol. 60, 2022, Art. no. 4303315.

[6] A. Benedikter, M. Rodriguez-Cassola, P. Prats-Iraola, G. Krieger, and G. Fischer, "On the processing of single-pass InSAR data for accurate elevation measurements of ice sheets and glaciers," *IEEE Trans. Geosci. Remote Sens.*, vol. 62, 2024, Art. no. 4300310.

[7] A. Kovacs, A. J. Gow, and R. M. Morey, "The in-situ dielectric constant of polar firn revisited," *Cold Regions Sci. Technol.*, vol. 23, no. 3, pp. 245–256, May 1995.

[8] M. Born et al., *Principles of Optics: Electromagnetic Theory of Propagation, Interference and Diffraction of Light*, 7th ed., Cambridge, U.K.: Cambridge Univ. Press, 1999.

[9] J. A. Sethian, "Fast marching methods," *SIAM Rev.*, vol. 41, no. 2, pp. 199–235, Jan. 1999.

[10] M. S. Hassouna and A. A. Farag, "MultiStencils fast marching methods: A highly accurate solution to the Eikonal equation on Cartesian domains," *IEEE Trans. Pattern Anal. Mach. Intell.*, vol. 29, no. 9, pp. 1563–1574, Sep. 2007.

[11] W. Carrara, R. Goodman, and R. Majewski, *Spotlight Synthetic Aperture Radar: Signal Processing Algorithms*. Norwood, MA, USA: Artech House, 1995.

[12] P. Prats, K. A. C. D. Macedo, A. Reigber, R. Scheiber, and J. J. Mallorqui, "Comparison of topography- and aperture-dependent motion compensation algorithms for airborne SAR," *IEEE Geosci. Remote Sens. Lett.*, vol. 4, no. 3, pp. 349–353, Jul. 2007.

[13] W. Kofman et al., "Properties of the 67P/churyumov-gerasimenko interior revealed by CONSERT radar," *Science*, vol. 349, no. 6247, p. 0639, Jul. 2015.

[14] C. M. Huber, A. Benedikter, G. Krieger, and M. Rodriguez-Cassola, "Radar travel time tomography for subsurface ice exploration at Saturn's moon Enceladus," in *Proc. 18th Eur. Radar Conf. (EuRAD)*, Apr. 2022, pp. 433–436.